RGO/Ag$_2$S/TiO$_2$ ternary heterojunctions with highly enhanced UV-NIR photocatalytic activity and stability

Tongyao Liu [a,b], Bin Liu [a,b,*], Linfen Yang [a,b], Xinlong Ma [a,b], Hao Li [a,b], Shu Yin [c], Tsugio Sato [c], Tohru Sekino [d], Yuhua Wang [a,b,*]

[a] Department of Materials Science, School of Physical Science and Technology, Lanzhou University, Lanzhou, 730000, China
[b] Key Laboratory of Special Function Materials and Structure Design, Ministry of Education, China
[c] Institute of Multidisciplinary Research for Advanced Materials, Tohoku University, 2-1-1 Katahira, Aoba-ku, Sendai, Japan
[d] The Institute of Scientific and Industrial Research, Osaka University, Japan

ARTICLE INFO

ABSTRACT

A series of novel RGO/Ag$_2$S/TiO$_2$ heterostructure photocatalysts has been synthesized successfully by a facial hydrothermal and simple ionexchange method. During the preparation, the reduction of graphene oxide (GO) and growth of TiO$_2$ and Ag$_2$S are accomplished smoothly, and the functions of each part are developed well together. Compared with pure TiO$_2$, Ag$_2$S and Ag$_2$S/TiO$_2$ nanocomposite, the obtained 3 wt.% RGO/Ag$_2$S/TiO$_2$ nanocomposite exhibits a significant enhancement of ultraviolet (UV) and near-infrared (NIR) light photocatalytic activities. Owing to its extended photoresponsive range, great adsorptive property and efficient electron-hole separation capacity. Furthermore, benefited by the introduction of reduced graphite oxide (RGO), the deterioration of Ag$_2$S is inhibited well and the stability of RGO/Ag$_2$S/TiO$_2$ nanocomposite has been enhanced greatly.

© 2016 Elsevier B.V. All rights reserved.

1. Introduction

Utilization of photocatalytic technology to solve the energy crisis and environmental contaminations has been thriving, owning to its clean, non-polluting and high-efficiency properties [1–3]. Up to now, UV and visible (Vis) light respond photocatalysts have been studied vastly and some excellent photocatalysts have been developed well. Titanium dioxide (TiO$_2$) has been widely employed as a photocatalyst because of its low cost, high photoinduced charge carries utilization efficiency and outstanding photocatalytic activity, but the narrow absorption band in UV region (which accounts for only 5% of the solar spectrum) astricts its practical application [4–6]. In order to utilize solar light more efficiently, modifying TiO$_2$ by surface modification [7,8], doping of metal or nonmetal elements [9–11], and combination with narrow band gap semiconductors to enhance the visible light absorption and photocatalytic activity has been a main research direction in recent years [12,13]. Nevertheless, the NIR light of large fraction (∼50%) in sunlight remains untapped since its low photon energy cannot directly give rise

to the response of most semiconductors during the solar energy conversion process [14]. In other words, the relative low-usage of sunlight has been restraining the photocatalytic efficiency in the environmental remediation, and the development of the NIR light excited photocatalysts to utilize solar light efficiently is an urgent task [6,15].

Lately, Jiang et al. have prepared Ag$_2$S by a simple ion-exchange method at room temperature and used it directly as a NIR light induced photocatalyst, but the narrow band gap about 0.9 eV leads to the fast recombination of photo carries and low photodegradation rate under the irradiation of different light [16,17]. Depending on the broad and strong absorption property of Ag$_2$S in the whole solar energy spectra, especially in NIR light region, the fabrication of heterojunction with TiO$_2$ is a good modification method to improve the charge carries transfer and separation capacity, and then enhance the photocatalytic activity [6,18]. In previous reports, there has been some positive results of Ag$_2$S-coupled TiO$_2$ composite in photocatalysis area. Zhu et al. have reported the photocatalytic activity of Ag$_2$S sensitized TiO$_2$ catalysts towards methylene blue photodegradation, and the nanocomposite exhibits much higher photocatalytic activity than that of pure Ag$_2$S and TiO$_2$ under visible light irradiation [19]. Furthermore, Gholami et al. have fabricated Ag$_2$S-TiO$_2$ nanotube arrays to split water and it exhibits about 15-fold photo-enhancement in current density as

---

compared with the pure TiO_2 nanotubes under similar conditions [20]. Regardless of these few reports on the visible-light-induced photocatalytic properties of Ag_2S modified TiO_2 composite, the photocatalytic activity of Ag_2S-TiO_2 system under the irradiation of NIR light has not been completely studied yet. Therefore, it is highly interesting and important to explore the potential of NIR photocatalytic activity of Ag_2S-TiO_2 composite, so as to utilize solar light more efficiently by responding in the extended solar energy spectra region.

In addition, the poor stable property of most Ag-containing compounds hinders the practical application of Ag_2S as a recyclable and highly efficient photocatalyst, because the Ag (I) could be reduced to metallic Ag by the photogenerated electrons under light irradiation [3,21–23]. Hence, it is important to accelerate the transfer of photogenerated electrons for higher photocatalytic stability. Reduced graphite oxide (RGO) has recently attracted intense scientific interest owing to its large specific surface area, high chemical stability and excellent electrons capture and transport properties [24–26]. Benefiting from these characteristics, some RGO-based photocatalysts have been carried out (e.g., RGO/Ag_3PO_4, Ag/AgCl/RGO and Cu_2O–RGO composite), and the stability has been promoted after the introduction of RGO owing to the enhancement of the transfer and separation of photogenerated carriers [24,27,28]. Meanwhile, under the inhibiting effort of the recombination of electron-hole pairs, the photocatalytic activity has enhanced distinctly in these composites. Therefore, it is favorable to fabricate RGO with unstable Ag_2S to improve its photocatalytic stability and enhance the activity simultaneously.

Inspired by the above discoveries, RGO-Ag_2S-TiO_2 ternary heterostructured composites are designed and prepared via a hydrothermal method combined with a facile ionexchange method, and applied to the photocatalytic degradation of a methyl orange (MO) solution under UV and NIR-light irradiation. It is found that the UV and NIR photocatalytic activities are improved significantly with Ag_2S assemble onto the TiO_2 nanoparticles. Furthermore, the content of RGO obviously affects the photocatalytic activity of RGO-Ag_2S-TiO_2 nanocomposite and the addition of RGO could enhance the photocatalytic stability of Ag_2S effectively. Subsequently, the possible mechanism for the enhanced photocatalytic activity and stability of RGO-Ag_2S-TiO_2 are thoroughly proposed based on the obtained experimental results.

2. Experimental

2.1. Preparation of RGO-TiO2 nanocomposite

A certain amount of graphene oxide (GO) was redispersed via the assist of ultrasonication in 30 mL deionized water to obtain the homogeneous suspension. Then, 7.5 mL absolute ethyl alcohol with 1.71 mL tetrabutyl titanate (TBOT) were added dropwise to the suspensions under vigorous stirring for 30 min. Finally, the above suspensions were transferred into 50 mL Teflon-lined autoclaves and maintained at 150 °C for 10 h. After this hydrothermal reaction, the suspensions were centrifuged at 17000 rpm followed by washing with distilled water and ethanol twice, and then dried in an oven at 80 °C for 2 h. For comparison, pure TiO_2 were synthesized under the same condition without the existence of GO.

2.2. Preparation of RGO-Ag2S-TiO2 nanocomposite

In a typical process, 0.4 g as-prepared RGO-TiO_2 nanocomposite and 0.34 g $AgNO_3$ were redispersed via the assist of ultrasonication in 40 mL deionized water to obtain the homogeneous suspension. After that, 30 mL aqueous solution with 0.24 g $Na_2S\cdot9H_2O$ was added dropwise into the above solution at room tempera-

ture. Finally, suspensions were centrifuged at 17000 rpm followed by washing with distilled water five times, and then dried under vacuum at 60 °C for 10 h. The nominal contents of GO additives were 1 wt.%, 3 wt.% and 5 wt.%, respectively for the RGO-Ag_2S-TiO_2 nanocomposite (RAT). These samples are labelled as 1RAT, 3RAT and 5RAT, respectively. For comparison, the Ag_2S-TiO_2 nanocomposite (AT) and bare Ag_2S were synthesized under the same condition.

2.3. Sample characterization

The phase purity of samples was analyzed by X-ray powder diffraction (XRD) using a Bruker D2 PHASER X-ray diffractometer with graphite monochromator using Cu Kα radiation (λ = 1.54184 Å) at room temperature. The energy dispersive X-ray spectroscopy (EDS) spectrum was detected by field emission scanning electron microscopy (FESEM, Hitachi, 30 S-4800). Moreover, transmission electron microscopy (TEM) with high-resolution transmission electron microscopy (HRTEM) and high angle annular dark field and scanning transmission electron microscopy (HAADF-STEM) were collected on an electron microscope (Tecnai™ G2 F30, FEI, US). X-ray photoelectron spectroscopy (XPS, PHI-5702, Physical Electronics) was performed using a monochromated Al Ka irradiation. The chamber pressure was $\sim 3 \times 10^{-8}$ Torr under testing conditions. Raman spectra of the samples were measured using a Renishaw inVia Raman microscope with 532 nm laser excitation. Besides, the UV–vis-NIR absorption spectra were measured with a Perkin Elmer Lambda 950 spectrometer. $BaSO_4$ was used as a reference with wavelengths in the 200–2500 nm range. The measurement of specific surface area was performed using nitrogen adsorption isotherm by Brunauer–Emmett–Teller surface analyzer (BET, ASAP2020 M, Micromeritics Instrument Corp, USA). Photoluminescence (PL) spectra were measured at room temperature using a FLS-920T fluorescence spectrophotometer equipped with a 450 W Xe light source and double excitation monochromators.

2.4. Evaluation of photocatalytic activity

The photocatalytic activities of the as-prepared samples were evaluated by measuring the degradation ratio of methyl orange (MO) solution under various light irradiation. A 500 W high pressure Hg lamp was employed for the ultraviolet irradiation source and 50 mg photocatalysts were suspended in the MO solution (10 mg/L, 80 mL). A diode laser of 980 nm with a power of 2 W was used as the irradiation source and 10 mg samples were suspended in the MO solution (10 mg/L, 20 mL). Before irradiation, the suspensions were stirred in the dark for 120 min to ensure the establishment of adsorption–desorption equilibrium. At varied irradiation time intervals, a certain volume of MO solution was withdrawn at selected times and analyzed by measuring the light absorption of the clear solution at 464 nm (λ_{max} for MO solution) using a spectrophotometer (LG-722SP).

2.5. Photoelectrochemical measurements

Photocurrent was measured on an electrochemical analyzer (CS 310, Wuhan Corrtest Instrument Co. Ltd.) in a standard three-electrode system using the pure TiO_2, Ag_2S/TiO_2 and 3 wt.% RGO-Ag_2S-TiO_2 nanocomposite (effective area was 1 cm^2) as working electrodes, a Pt foil and an Ag/AgCl (saturated KCl) electrode were used as the counter electrode and reference electrode, respectively. The photoanode was suspended into Na_2SO_4 (0.1 mol L^{-1}) aqueous solution with a 300 W Xe arc lamp equipped a UVREF filter (200–400 nm) served as a UV-light source and the diode laser of 980 nm with a power of 2 W provides NIR light. All electrochemical experiments were carried out at room temperature with light
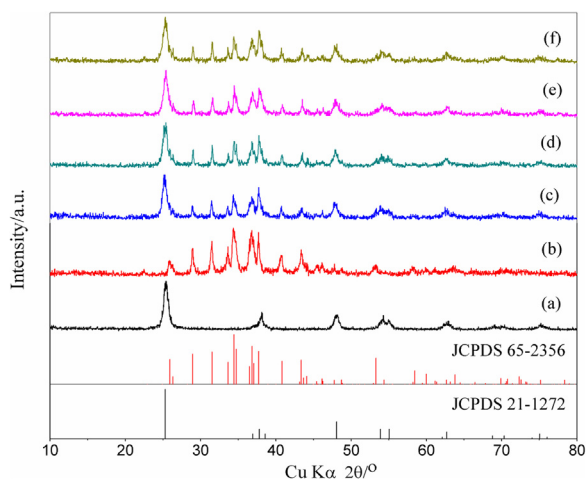
Fig. 1. XRD patterns of (a) pure TiO$_2$, (b) pure Ag$_2$S, (c) AT and different RAT nanocomposites: (d) 1RAT, (e) 3RAT and (f) 5RAT.

ON−OFF switches of 4 s at a constant potential of 0 V to the reference electrode. The electrochemical impedance spectroscopies (EIS) of as-prepared samples were carried out at the open circuit potential. The frequency was ranging from 0.01 Hz to 100000 Hz and the amplitude of the sinusoidal wave was 10 mV. The flat-band potentials (V$_{fb}$) were determined from Mott–Schottky plots by electrochemical method in Na$_2$SO$_4$ solution (0.1 mol L^{-1}). The Mott–Schottky measurements were performed at a fixed frequency of 1000 Hz with 10 mV amplitude, at various applied potentials.

3. Results and discussion

Fig. 1 presents the XRD patterns of the pure TiO$_2$, Ag$_2$S, AT and RAT nanocomposites with different RGO ratios. The reflection in Fig. 1a matches best with the single anatase TiO$_2$ phase (JCPDS 21–1272). Moreover, XRD pattern from the AT nanostructures (Fig. 1c) obviously consists of two sets of diffraction peaks.

Compared to the peaks of the anatase TiO$_2$, there are three sharp diffraction peaks at 2θ values of 34.4°, 36.8° and 37.7°, which could be indexed to the ($\bar{1}$21), (121) and ($\bar{1}$03) crystal planes of Ag$_2$S (JCPDS 65–2356), respectively, and these peaks reveal that the Ag$_2$S nanocrystallites are actually deposited on the AT nanocomposite. Notably, in the RAT composites, peaks for RGO are not clearly visible, which is attributed to the two-dimensional thin graphene layers could not be detected by the XRD instrument [29]. Meanwhile, no additional diffraction peaks corresponding to any impurity phase is observed in the synthesized samples, which indicates that the high-purity property of RAT nanocomposites.

The microscopic morphologies and structures of TiO$_2$, AT and 3RAT are observed via TEM. It can be observed from Fig. 2a that the TiO$_2$ nanocrystallite appears in an agglomerated status and the size of the primary particles estimated from the TEM image is about 13 nm. Fig. 2b shows that the Ag$_2$S nanoparticles are randomly coated on the TiO$_2$ nanoparticles, and the relatively homogenous dispersion of Ag$_2$S in the matrix of TiO$_2$ will promote the formation of TiO$_2$/Ag$_2$S nanojunctions. Furthermore, the two-dimensional structure of RGO with some wrinkles could be clearly observed in RGO/TiO$_2$/Ag$_2$S as displayed in Fig. 2c, and the TiO$_2$ nanoparticles as well as Ag$_2$S are well-decorated on or intercalated into the RGO sheets to form a ternary heterojunction. Moreover, to further confirm the co-presence of the TiO$_2$ and Ag$_2$S in RGO/TiO$_2$/Ag$_2$S nanocomposites, the HRTEM of the magnified view is employed and displayed in Fig. 2d. The measured lattice spacing for the crystalline plane of 0.35 nm and 0.34 nm can be assigned to the (101) plane of anatase TiO$_2$ and the (101) plane of Ag$_2$S nanocrystals, respectively. Obviously, the high density of the Ag$_2$S is expected to enhance optical absorption in the UV and NIR light wavelength, and the high transmission efficiency of charge carriers which caused by RGO will lead to an enhancement of the carrier separation capacity under the irradiation of UV and NIR light. In addition, the elemental composition of 3RAT has been investigated by EDX spectrum (insert Fig. 2d) and elemental mapping analysis (Fig. 2e and f). Clearly, the homogeneous distribution of Ti, O, Ag and S elements suggests that Ag$_2$S combined well with TiO$_2$, and the coexistence of Ag$_2$S,
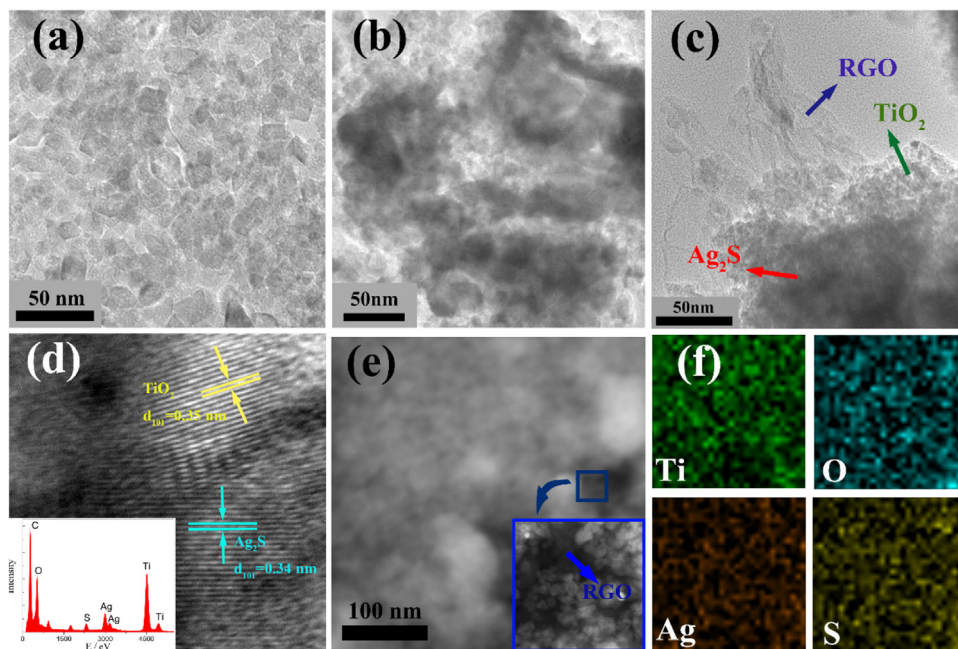

Fig. 2. TEM images of the obtained (a) TiO$_2$, (b) AT and (c) 3RAT. (d) The HRTEM images of as-synthesized 3RAT nanocomposite and the inset shows EDX spectrum of 3RAT nanocomposite. (e) The element distribution map of a STEM image (inset is the high-magnification STEM image of the selected region) and (f) the presence of Ti, O, Ag and S elements on the 3RAT nanocomposite.
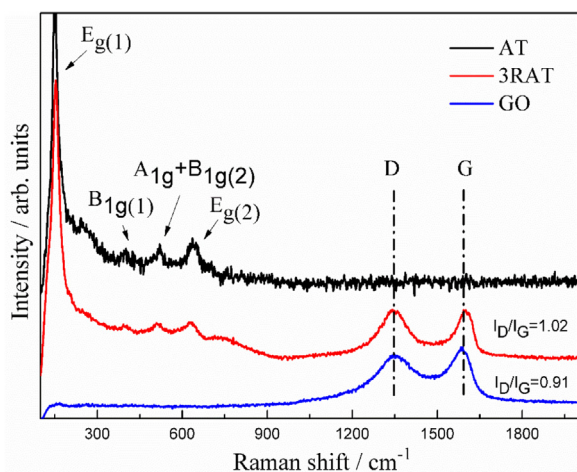
Fig. 3. Raman spectra of the GO, AT and 3RAT samples.

TiO_2 and RGO will greatly accelerate the synergistic effect in RAT nanocomposites.

Raman spectroscopy is a powerful tool to characterize the crystalline quality of carbon and can be used to prove the co-existence of TiO_2 and RGO in the RGO/TiO_2/Ag_2S nanocomposites. Fig. 3 shows a comparison of the Raman spectra of GO, AT and 3RAT nanocomposite. GO shows a Raman shift at 1350 and 1589 cm^{-1} corresponding to the D and G bands, respectively, and the D/G intensity ratio of GO is 0.91 [30]. As for AT composite, several characteristic bands at 153, 400, 520 and 636 cm^{-1} correspond to the $E_{g(1)}$, $B_{1g(1)}$, A_{1g} + $B_{1g(2)}$ and $E_{g(2)}$ modes of anatase, respectively [31]. When it comes to the 3RAT nanocomposite, besides the bands attributed to the anatase vibrations, two characteristic peaks at about 1343 cm^{-1} (D band) and 1593 cm^{-1} (G band) for the graphitized structures are observed, suggesting the co-existence of TiO_2 and RGO in the RGO/TiO_2/Ag_2S

nanocomposites. Notably, the value of D/G intensity ratio increases to 1.02 in this nanocomposite. The increase in the intensity of D/G intensity ratio indicates the decrease of the oxygen-functional groups on GO, which further confirms that the GO has been effectively reduced to RGO during the hydrothermal reaction.

The surface chemical compositions and bonding states of GO and 3RAT nanocomposite are further analyzed by XPS. It is obviously seen that, in Fig. 4a, only elements of Ti, O, Ag, S and C can be found in spectra of the nanocomposite, and no other impurities are detectable. Fig. 4b shows the high-resolution C 1 s XPS spectrum of GO. Five typical peaks of GO are located at 284.6, 285.8, 286.8, 287.8 and 288.9 eV, which are assigned to the sp^2 bonded carbon (C—C), defect-containing sp^2-hybridized carbons, epoxy/hydroxyls (C—O), carbonyls (C=O) and carboxyl (O—C=O), respectively, indicating the high percentage of oxygen-containing carbon in GO [32,33]. These oxygen-containing functional groups will promote the connection between GO sheets and TiO_2 nanoparticles, so as to facilitate the electron transfer during the photocatalytic process [34]. After hydrothermal treatment of GO nanosheets, the chemical state of the carbon atoms in the hexagonal lattice of graphene is also characterized and displayed in Fig. 4c. By contrast, most of the oxygen-containing species (e.g. C—O, C=O et al) are removed and the majority of the conjugated C networks are restored. Moreover, the slightly increased carboxyl peak at 288.9 eV could be attributed to the —OH groups on the TiO_2 reacted with the O—C=O groups on the GO surface through esterification to form O=C—O—Ti bonds [34]. The above results further confirm the effective reduction of GO in RGO/TiO_2/Ag_2S nanocomposites and the interfacial connection between GO sheets and TiO_2 nanoparticles, which is corresponding well to the Raman spectra (Fig. 3). Furthermore, the high-resolution XPS spectrum of Ag 3d for 3RAT samples is shown in Fig. 4d. The peaks at 373.6 and 367.6 eV are assigned to Ag $3d_{3/2}$ and Ag $3d_{5/2}$ of Ag^+ ions in Ag_2S, respectively [35,36]. These results further indicate the close combination among RGO, Ag_2S and TiO_2.
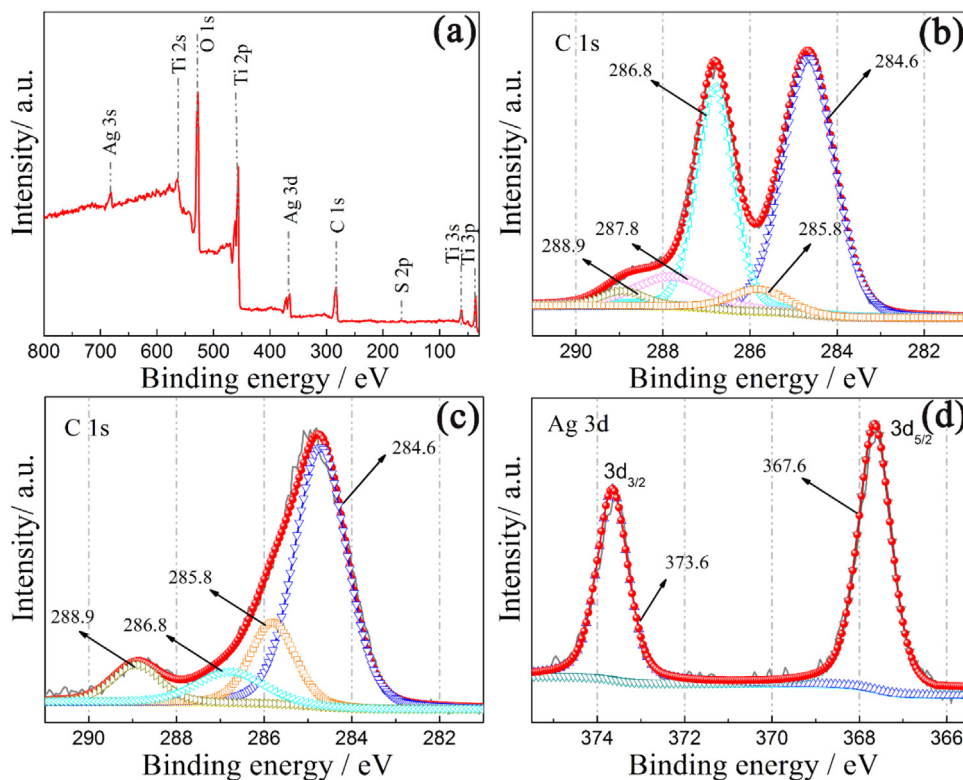

Fig. 4. (a) Full XPS spectra of 3RAT nanocomposite. High-resolution XPS spectra of C 1 s for (b) GO, (c) 3RAT and (d) Ag 3d for 3RAT samples.
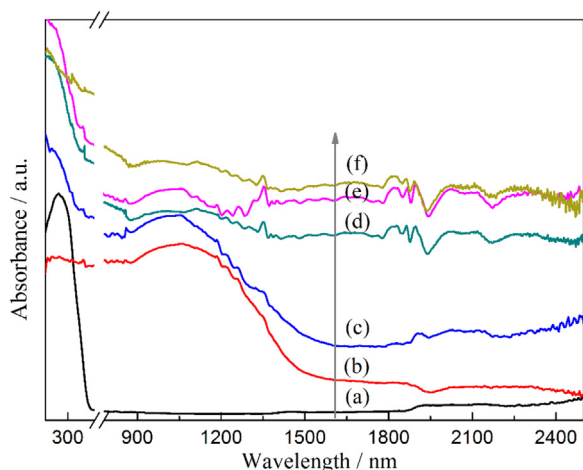
Fig. 5. UV-NIR absorption spectra of (a) pure TiO_2, (b) pure Ag_2S, (c) AT and different RAT nanocomposites: (d) 1RAT, (e) 3RAT and (f) 5RAT.

The optical property plays an important role in determining the photocatalytic activity. The UV (200–420 nm)-NIR (780–2500 nm) absorption spectra of the as prepared TiO_2, Ag_2S, AT and RAT nanocomposites with different RGO ratios are listed in Fig. 5. TiO_2 shows a strong absorption in the UV region, and the Eg of TiO_2 is approximately 3.2 eV, which corresponds to the absorption of wavelength <380 nm. As for Ag_2S particles, the spectrum shows a broad and strong light absorption in the UV and NIR region, while the absorption edge extends to ~1400 nm, which is corresponding bandgap energy of 0.9 eV. With the introduction of Ag_2S onto the surface of TiO_2 nanoparticles, the AT nanocomposite exhibit a remarkable absorption enhancement in the UV region and the absorption spectra are successfully extended to NIR light region compared with bare TiO_2 nanoparticles. This phenomenon suggests that the heterostructured AT nanocomposite have a potential photocatalytic activity under irradiation of UV and NIR light. Significantly, the improved absorption of the RAT nanocomposites in the UV-NIR light region and an obvious red shift of the absorption edge could be observed in comparison with bare AT or TiO_2. Besides, with increasing amount of the RGO, the RAT composites show a continuously enhanced absorption in the range upon 780 nm, indicating a more efficient utilization of the solar light could be achieved in RAT nanocomposites. Therefore, compared with bare TiO_2, Ag_2S and AT samples, a better photochemical response under UV and NIR light irradiation is expected in RAT nanocomposites.

To prove the photocatalytic activity of the RAT nanocomposites, the decomposition of MO solution in water under UV and NIR light irradiation as a function of irradiation time are investigated. For comparison, the photocatalytic activity of TiO_2, Ag_2S and AT composite are tested under the same experimental conditions. Before the photocatalysis, the suspension is stirred for 120 min in the dark to reach the adsorption–desorption equilibrium. As displayed in Fig. S1, the RAT nanocomposites show obvious higher adsorption property than TiO_2, Ag_2S as well as AT composite, which could be attributed to the higher BET surface area of RGO/Ag_2S/TiO_2 (e.g. the BET surface area of 3RAT is 135.96 m^2/g) than that of AT (115.54 m^2/g). The higher adsorption capacity could lead to the easier and faster photocatalytic degradation process because the photocatalytic reaction is a surface-based process. As shown in Fig. 6a, nearly no photolysis of MO solution is observed after NIR light irradiation for 180 min with the absence of photocatalysts, and the temperature of MO solution only increases 0.3 °C after NIR light irradiation for 180 min (Fig. S2). These phenomena demonstrate the photo-thermal effect can be ignored in the NIR light photocatalytic degradation [37,38]. Moreover, no degradation of

MO solution is observed with the existence of TiO_2, indicating TiO_2 has no NIR photodegradation ability. As for Ag_2S samples, only 6% of the MO solution is photodegraded after 180 min of irradiation. After Ag_2S assemble onto the TiO_2 nanoparticles, the AT composite can respond to NIR light effectively and about 42% of MO solution can be degraded in 180 min. The enhanced NIR photocatalytic activity of AT composite implies the effective interaction between TiO_2 and Ag_2S as discussed in Fig. 2. Notably, compared with AT composite, the RAT nanocomposites exhibit higher NIR light photocatalytic activity and the degradation rate generated increases with the increase in the graphene content. However, the photocatalytic activity reached the maximum when the graphene content reached 3 wt.%, and a further increase in the graphene content led to a deterioration of the catalytic performance, even if the 5RAT sample shows stronger absorption in the wavelength of NIR region and higher adsorption capacity of dyes. It is reasonable because the introduction of a large percentage of black RGO could lead to a shield of the active sites on the photocatalyst surface [39]. Moreover, with regard to UV light photodegradation (Fig. 6b), no photolysis of MO is observed after 30 min UV light irradiation with the absence of photocatalysts, and similar phenomena have been observed in the case of AT and RAT nanocomposites: the photocatalytic degradation efficiency under UV light follows the order 3RAT > 5RAT ~ 1RAT > AT > TiO_2 > Ag_2S. For instance, about 98% of the initial MO molecules are decomposed by the 3RAT nanocomposite, while only 48% and 62% by the bare TiO_2 and AT within 10 min. These above results clearly demonstrate the introduction of Ag_2S and RGO into TiO_2 can actually extend the nanocomposites sensitive to the NIR region and increase the utilization of solar light, because of the effective synergistic effects among TiO_2, Ag_2S and RGO.

As we all know, the value of photocurrent offers an informative evaluation of the efficiency of charge generation and separation under irradiation [40]. In order to prove the positive effect of Ag_2S and RGO on the elevated photocatalytic activity of AT and RAT nanocomposites, the photocurrent measurements of pure TiO_2, pure Ag_2S, AT and RAT are carried out under selective light illumination conditions. As shown in Fig. 7a, when the UV light on, an apparent rise in the photocurrent responses can be discerned for all the electrodes, and the on–off cycles of the photocurrents are reproducible. It could be clearly seen that the photocurrent decreases with the order of 3RAT > AT > TiO_2 > Ag_2S, and the photocurrent value of 3RAT electrode reached as high as 46.7 μA/cm^2, which is 5.7 times than that of pure TiO_2 (8.2 μA/cm^2). However, the pure TiO_2 showed almost no photocurrent response with the NIR light irradiation and Ag_2S processed only slight change under the irradiation of NIR light as displayed in Fig. 7b. As expected, after the introduction of Ag_2S and RGO into TiO_2, the AT and 3RAT nanocomposite show a significant photocurrent intensity enhancement when the NIR light irradiated. The 3RAT hybrid shows the highest photocurrent intensity (2.54 μA/cm^2), which is more than 3.4 times than that of pure Ag_2S (0.75 μA/cm^2) and 1.4 times than that of AT composite (1.81 μA/cm^2). The above results further prove the efficient separation of photogenerated charge carriers in 3RAT samples, which could be attributed to fabrication of the RGO/Ag_2S/TiO_2 heterojunction.

Meanwhile, in the presence of 3RAT and AT samples, the photocurrent values increase to the maximum value more slowly those that of bare Ag_2S and TiO_2 when the light is on, and tardily come back to zero when the light is off. This difference of the I-t curves can be attributed to the special electron transfer process. In AT sample, the formation of Ag_2S/TiO_2 heterojunction accelerates the transfer of photogenerated electrons from Ag_2S to TiO_2. Under the circumstances, the photocurrent is not only generated by electrons from the CB of Ag_2S and TiO_2, but also generated by some transferred electrons between Ag_2S to TiO_2. Therefore, the response
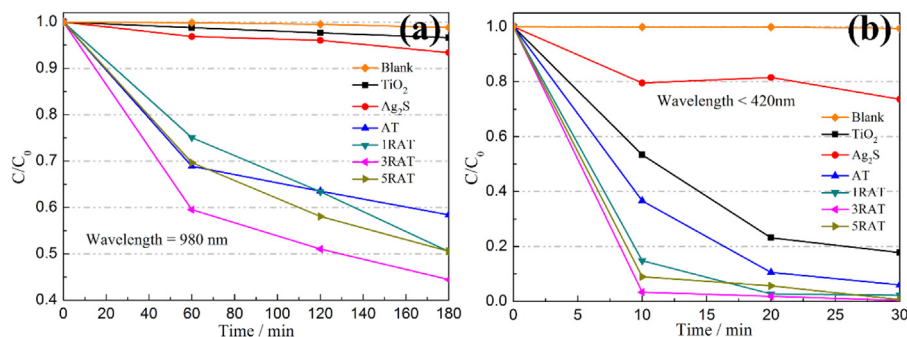
Fig. 6. Variation of MO solution concentration against irradiation time using TiO_2, Ag_2S, AT and different RAT nanocomposites under (a) NIR and (c) UV light irradiation. Plots of ln (C_0/C) versus (b) NIR and (d) UV light irradiation time for MO solution representing the fit using a pseudo-first-order reaction rate.
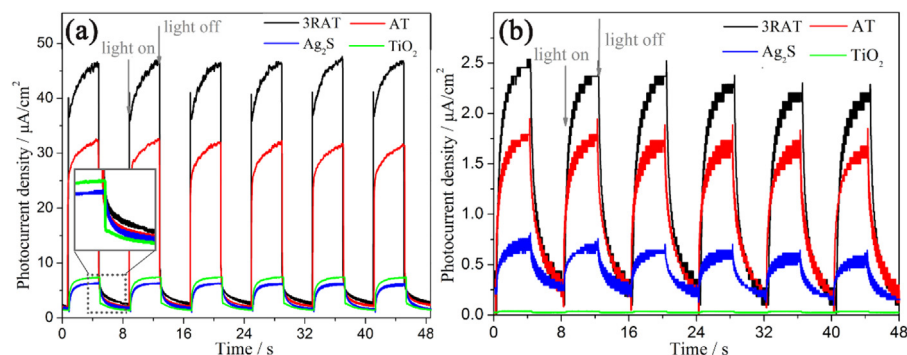

Fig. 7. Photocurrent density vs. time (I–t) curves of TiO_2, Ag_2S, AT and 3RAT nanocomposite under (a) UV and (b) NIR light illumination conditions.

speed of photocurrent values will be delayed slightly when the light is switched on and off (Fig. 7a) [41,42]. Moreover, with the further addition of RGO into AT sample, the photogenerated electrons on the conduction band (CB) of TiO_2 tend to farther transfer to the surface of RGO. Thus, the photocurrent will be generated by stored electrons from RGO instead of the CB of TiO_2 directly, resulting in the slowly increasement of photocurrent values. Similarly, when the light is off, the stored electrons will be released from RGO gradually and further transfer to working electrode, leading to the photocurrent values tardily come back to zero [43,44]. In this situation, the life time of photogenerated charge carriers may been prolonged efficiently in 3RAT, and then improve the photocatalytic activities significantly.

It has been demonstrated that the optical properties of solid materials are closely related to their microstructure, PL and EIS analyses are always used to reveal the migration, transfer, and separation efficiency of the photogenerated electrons and holes in semiconductors [32,45]. The comparison of PL spectra of TiO_2, AT and 3RAT nanocomposite excited at 300 nm is shown in Fig. 8a [46]. As can be seen, all samples show three PL intensity peaks at 407 nm, 470 nm, 494 nm. The broad emission peak at 407 nm can be well separated into four small peaks locating at 397, 407, 423 and 438 nm. According to the reports, the peak at 397 nm could be attributed to the band–band PL phenomenon with the energy of light approximately equal to the band gap energy of anatase (392.4 nm) [47,48]. Other peaks in the broad emission peak are attributed to excitonic PL, which mainly result from surface oxygen vacancies and defects of semiconductors [49,50]. Furthermore, the PL peak at 470 nm is attributed to band edge free excitons while the peak at 494 nm can be attributed to bound excitons [51]. Since the PL intensity follows the order $TiO_2 > AT > 3RAT$ (as the typical RAT nanocomposite). Considering the lower PL intensity indicates the lower recombination rate of charge carriers and higher photocatalytic activity, the 3RAT nanocomposite is favorable to accelerate

the separation of electron-hole pairs and then improves its photodegradation ability.

Meanwhile, EIS is employed to further confirm the positive effect of the RGO on the dynamics of interfacial charge transfer under different conditions. The smaller radius of the Nyquist circle represents the lower charge transfer resistance [52,53]. As presented in Fig. 8b and Fig. S3, the 3RAT nanocomposite displays the smallest arc radius in dark or under UV, NIR-light irradiation compared with bare Ag_2S, TiO_2 and AT samples. This result indicates the introduction of appropriate RGO into AT is an efficiency way to facilitate the photogenerated electron–hole pairs separation and the interfacial charge transfer, which is consistent with the results of PL spectra.

To investigate the stability of AT and the 3RAT nanocomposite, we repeated the photodegradation of the MO solution with the photocatalysts four times under the same condition, and the corresponding results are shown in Fig. 9a. Obviously, the photocatalytic performance of AT shows an obvious less, and the degradation rate of AT decreases to 61% after four cycles. However, when involving RGO sheets into the composite, the photocatalytic efficiency of the 3RAT nanocomposite only displays slight decreases after the reaction is performed consecutively four times, which could be attributed to the catalyst dissolved and lost during the photocatalytic reaction process due to its good dispersibility [54]. Moreover, as revealed in Fig. 9b, except the peaks at 373.7 and 367.7 eV which are assigned to Ag 3d3/2 and Ag 3d5/2 of Ag^1 ions, where those at 374.5 and 368.5 eV are indexed to the Ag 3d3/2 and Ag 3d5/2 of metallic Ag that reduced by the photoinduced electrons during the MO solution degradation process [35]. By comparison, the relative percentage of Ag^0 is 33.1% while that of Ag^1 is 66.9% in the AT samples after four cycle degradation, whereas 3RAT showed only 8.3% Ag^0 and more Ag^1 (91.7%) in the same condition. It could be clarified that the incorporation of RGO sheets leads to the positive synergistic effects between RGO and AT composite, and the reduction of
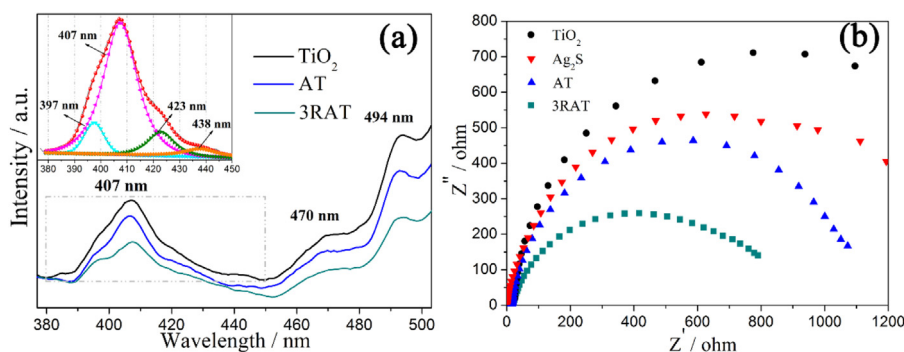
Fig. 8. (a) Photoluminescence (PL) spectra of TiO_2, AT and 3RAT nanocomposite: $\lambda_{ex} = 300$ nm. The insert shows the fitting of the emission band from 380 nm to 450 nm. (b) EIS Nyquist plots of TiO_2, Ag_2S, AT and 3RAT nanocomposite in the dark.
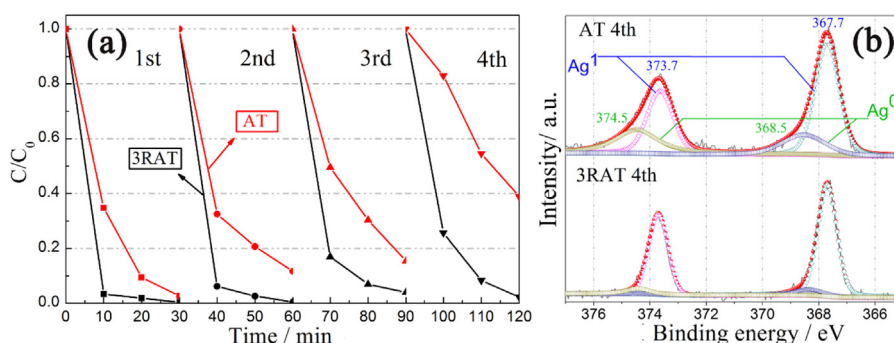

Fig. 9. (a) Repeated photocatalytic degradation of MO solution under UV light irradiation (red line: AT nanoparticles; black line: 3RAT nanocomposite); (b) High-resolution XPS spectra of Ag 3d for AT and 3RAT nanocomposite after the fourth cycle experiments. (For interpretation of the references to colour in this figure legend, the reader is referred to the web version of this article.)

Ag^1 to Ag^0 could be has been suppressed effectively. Consequently, the 3RAT nanocomposite is a great structural stabile photocatalyst, which is beneficial for the applications in water purification.

Generally, active species, such as holes, $\bullet O_2^-$, and $\bullet OH$ radicals are involved in the photodegradation process, and it is important to investigate the contributions of these oxidative species and elucidate the photocatalytic mechanism. Therefore, the trapping experiments of radicals and holes are carried out under UV or NIR light irradiation with the existence of $Na_2C_2O_4$ (hole scavenger), purging N_2 ($\bullet O_2^-$ scavenger), and t-BuOH ($\bullet OH$ scavenger), respectively [55,56]. As displayed in Fig. S4a, under UV light irradiation, the degradation efficiencies of 3RAT nanocomposite decrease slightly with the addition of t-BuOH (75.1%) and N_2 (74.1%), while it has been greatly prevented by $Na_2C_2O_4$ (30.9%), indicating the photogenerated holes are the main active species while $\bullet OH$ and $\bullet O_2^-$ radicals play an assistant role on the degradation of MO solution. Meanwhile, it can be seen that under the irradiation of NIR light (Fig. S4b), the degradation efficiencies are also obviously suppressed by $Na_2C_2O_4$ (7.7%) and N_2 (25.8%), but nearly no inhibiting effect exhibited with the addition of t-BuOH (47.1%). This result also suggests the direct hole oxidation govern the photocatalytic process under NIR light irradiation.

Based on the above discussion, the enhanced UV and NIR photocatalytic activities of 3RAT nanocomposite are contributed to the improvement capacity of light absorption and efficient separation of photo-induced carriers. To clarify the possible mechanism of the enhancement of photocatalytic activity, the positions of CB and valence band (VB) of TiO_2 and Ag_2S are determined by flat-band potentials (V_{fb}) and UV–vis-NIR absorption spectra, as displayed in Fig. S5. Positive slopes of Mott–Schottky plots indicate that both TiO_2 and Ag_2S are n-type, which is corresponding with the pre-

viously reported result [14,57]. The V_{fb} can be quantified by the Mott–Schottky equation:

$$1/C^2 = 2 \left(V - V_{fb} - kT/e \right) / \varepsilon \varepsilon_0 eN$$

where C is the total measured capacitance, V is the electrode applied potential, V_{fb} is the flat band potential, ε_0 is the vacuum permittivity, ε the dielectric constant of the material, e is the electron charge, k is the Boltzmann constant, T is the temperature, and N is the acceptor concentration. According to the Mott–Schottky equation, a linear relationship of C^{-2} vs. V can be observed (Fig. S5a and b) and the intercepts of the straight lines with the potential axis indicate the V_{fb} values of TiO_2 and Ag_2S are −0.13 V vs NHE and −0.21 V vs NHE[58], thus the CB of TiO_2 and Ag_2S are −0.33 V vs NHE and −0.41 V vs NHE, respectively [59]. Furthermore, combining with the bandgap energy of TiO_2 (∼3.16 eV) and Ag_2S (∼0.84 eV) as displayed in Fig. S5c and d, the energy level diagrams of 3RAT heterojunction with the presence of TiO_2, Ag_2S and RGO sheets are obtained and displayed in Fig. 10. Under UV light irradiation, both TiO_2 and Ag_2S could be excited to generate electrons and holes. Electrons photoexcited from Ag_2S transfer to the CB of TiO_2, and holes photoexcited from TiO_2 transfer from the VB of TiO_2 to that of Ag_2S. This transfer process is thermodynamically advantageous because both the CB and VB of Ag_2S are more negative than those of TiO_2. Moreover, RGO sheets, with a 2D conjugated π structure and excellent conductivity, act as good electron acceptors that it could accept the photogenerated electrons from CB of TiO_2. Under the circumstances, more effective transfer and separation of the photoinduced charges between TiO_2 and Ag_2S interfaces, resulting in markedly improved UV photocatalytic activity. When the 3RAT nanocomposite is irradiated by NIR light, only Ag_2S could act as a sensitizer benefits by its narrow band gap. Under NIR light illu-
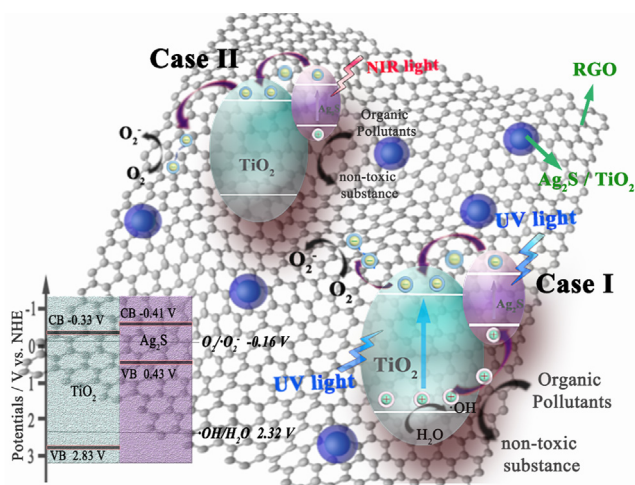
Fig. 10. Schematic diagram of band gap matching and flow of photo-induced carriers in the 3RAT heterojunction under UV and NIR light irradiation.

mination, electrons in the VB of Ag_2S could be excited to a higher CB, and then transfer to the CB of TiO_2 and finally to the surface of RGO sheets. In this process, the electrons could absorb some surface molecules such as O_2 and convert to oxidative species (O^{2-}). Meanwhile, the photogenerated holes accumulated in the VB of Ag_2S will accelerate the decomposition of organic pollutants into non-toxic substance, rather than generate the stronger oxidative species ($\bullet OH$), owing to the potential of $\bullet OH/H_2O$ (2.32 V vs NHE) is more positive than the VB of Ag_2S (0.43 V vs NHE) [60]. In such a way, the photoinduced electrons and holes could be separated effectively, so as to settle the high recombination probability of the photo-induced carriers in Ag_2S and greatly enhance photocatalytic activity under NIR light irradiation. Furthermore, rely on the outstanding electron transfer ability of RGO sheets, the stability of 3RAT nanocomposite will sustain well by keeping electrons away from Ag_2S and inhibiting deterioration during the photocatalysis process.

4. Conclusion

In summary, we have proposed and proven a new strategy by introducing the Ag_2S with wide spectrum absorption property and RGO sheets with excellent ionic conductivity into high-efficiency TiO_2 to extend the photoresponsive range and enhance the photocatalytic activity. Specifically, a series of RGO-Ag_2S-TiO_2 heterojunctions with good photocatalytic performance has been realized via a facial hydrothermal and simple ionexchange method. The enhanced UV-NIR photocatalytic activity could be associated with the favorable synergistic effects among RGO, Ag_2S and TiO_2 materials, such as large extended absorption of solar light, high electron–hole separation efficiency and strong adsorptivity of pollutants. More than that, the RAT nanocomposites are more stable than pure AT composite since the excellent electron-accepting and −transporting properties of RGO sheets, which could act as a covering layer to inhibit the deterioration of Ag_2S. Above all, RAT nanocomposites, especially for 3RAT, has great potential in making better use of solar energy to address various environmental issues more effectively.

Acknowledgements

Appendix A. Supplementary data

Supplementary data associated with this article can be found, in the online version, at http://dx.doi.org/10.1016/j.apcatb.2016.12.011.

References

[1] Y. Sang, H. Liu, A. Umar, ChemCatChem 7 (2015) 559–573.
[2] N. Wei, H. Cui, Q. Song, L. Zhang, X. Song, K. Wang, Y. Zhang, J. Li, J. Wen, J. Tian, Appl. Catal. B: Environ. 198 (2016) 83–90.
[3] X. Ma, H. Li, Y. Wang, H. Li, B. Liu, S. Yin, T. Sato, Appl. Catal. B: Environ. 158–159 (2014) 314–320.
[4] W. Qin, D. Zhang, D. Zhao, L. Wang, K. Zheng, Chem. Commun. 46 (2010) 2304–2306.
[5] M. Murdoch, G.I. Waterhouse, M.A. Nadeem, J.B. Metson, M.A. Keane, R.F. Howe, J. Llorca, H. Idriss, Nat. Chem. 3 (2011) 489–492.
[6] J. Tian, Y. Sang, G. Yu, H. Jiang, X. Mu, H. Liu, Adv. Mater. 25 (2013) 5075–5080.
[7] M.G. Méndez-Medrano, E. Kowalska, A. Lehoux, A. Herissan, B. Ohtani, D. Bahena, V. Briois, C. Colbeau-Justin, J.L. Rodríguez-López, H. Remita, J. Phys. Chem. C 120 (2016) 5143–5154.
[8] S. Wooh, T.Y. Kim, D. Song, Y.G. Lee, T.K. Lee, V.W. Bergmann, S.A. Weber, J. Bisquert, Y.S. Kang, K. Char, ACS Appl. Mater. Interfaces 7 (2015) 25741–25747.
[9] C. Sotelo-Vazquez, N. Noor, A. Kafizas, R. Quesada-Cabrera, D.O. Scanlon, A. Taylor, J.R. Durrant, I.P. Parkin, Chem. Mater. 27 (2015) 3234–3242.
[10] W. Zhou, H. Fu, ChemCatChem 5 (2013) 885–894.
[11] L.G. Devi, R. Kavitha, Appl. Catal. B: Environ. 140–141 (2013) 559–587.
[12] K. Li, B. Chai, T. Peng, J. Mao, L. Zan, ACS Catal. 3 (2013) 170–177.
[13] W. Zhou, Z. Yin, Y. Du, X. Huang, Z. Zeng, Z. Fan, H. Liu, J. Wang, H. Zhang, Small 9 (2013) 140–147.
[14] Y. Li, L. Li, Y. Gong, S. Bai, H. Ju, C. Wang, Q. Xu, J. Zhu, J. Jiang, Y. Xiong, Nano Res. 8 (2015) 3621–3629.
[15] W. Gao, W. Liu, Y. Leng, X. Wang, X. Wang, B. Hu, D. Yu, Y. Sang, H. Liu, Appl. Catal. B: Environ. 176–177 (2015) 83–90.
[16] W. Jiang, Z. Wu, X. Yue, S. Yuan, H. Lu, B. Liang, RSC Adv. 5 (2015) 24064–24071.
[17] Z.-D. Meng, T. Ghosh, L. Zhu, J.-G. Choi, C.-Y. Park, W.-C. Oh, J. Mater. Chem. 22 (2012) 16127.
[18] H. Feng, T. Tran, T.L. Chen, L. Yuan, Q. Cai, Chem. Eng. J. 215–216 (2013) 591–599.
[19] L. Zhu, Z. Meng, G. Trisha, W.-C. Oh, Chin J. Catal. 33 (2012) 254–260.
[20] M. Gholami, M. Qorbani, O. Moradlou, N. Naseri, A.Z. Moshfegh, RSC Adv. 4 (2014) 7838.
[21] G. Li, Y. Wang, L. Mao, RSC Adv. 4 (2014) 53649–53661.
[22] J.H. Kennedy, C. Fred, J. Electrochem. Soc. 116 (1969) 207–211.
[23] Y. Hou, F. Zuo, Q. Ma, C. Wang, L. Bartels, P. Feng, J. Phys. Chem. C 116 (2012) 20132–20139.
[24] C. Cui, Y. Wang, D. Liang, W. Cui, H. Hu, B. Lu, S. Xu, X. Li, C. Wang, Y. Yang, Appl. Catal. B: Environ. 158–159 (2014) 150–160.
[25] B. Qiu, Y. Deng, M. Du, M. Xing, J. Zhang, Sci. Rep. 6 (2016) 29099.
[26] B. Qiu, Q. Li, B. Shen, M. Xing, J. Zhang, Appl. Catal. B: Environ. 183 (2016) 216–223.
[27] P.D. Tran, S.K. Batabyal, S.S. Pramana, J. Barber, L.H. Wong, S.C. Loo, Nanoscale 4 (2012) 3875–3878.
[28] G. Luo, X. Jiang, M. Li, Q. Shen, L. Zhang, H. Yu, ACS Appl. Mater. Interfaces 5 (2013) 2161–2168.
[29] G. Jiang, Z. Lin, C. Chen, L. Zhu, Q. Chang, N. Wang, W. Wei, H. Tang, Carbon 49 (2011) 2693–2701.
[30] B. Liu, S. Yin, X. Wu, Y. Wang, Y. Huang, J. Wu, T. Sekino, J. Matsushita, S.W. Lee, M. Kobayashi, M. Kakihana, T. Sato, Carbon 94 (2015) 309–316.
[31] J. Qiu, P. Zhang, M. Ling, S. Li, P. Liu, H. Zhao, S. Zhang, ACS Appl. Mater. Interfaces 4 (2012) 3636–3642.
[32] Y. Ping, J.-M. Yan, Z.-L. Wang, H.-L. Wang, Q. Jiang, J. Mater. Chem. A 1 (2013) 12188.
[33] Q. Li, B. Guo, J. Yu, J. Ran, B. Zhang, H. Yan, J.R. Gong, J. Am. Chem. Soc. 133 (2011) 10878–10884.
[34] Q. Xiang, J. Yu, M. Jaroniec, Nanoscale 3 (2011) 3670–3678.
[35] N. Feng, Q. Wang, A. Zheng, Z. Zhang, J. Fan, S.B. Liu, J.P. Amoureux, F. Deng, J. Am. Chem. Soc. 135 (2013) 1607–1616.
[36] X. Yang, H. Xue, J. Xu, X. Huang, J. Zhang, Y.B. Tang, T.W. Ng, H.L. Kwong, X.M. Meng, C.S. Lee, ACS Appl. Mater. Interfaces 6 (2014) 9078–9084.

[37] X. Guo, W. Song, C. Chen, W. Di, W. Qin, Phys. Chem. Chem. Phys. 15 (2013) 14681–14688.
[38] X. Guo, W. Di, C. Chen, C. Liu, X. Wang, W. Qin, Dalton Trans. 43 (2014) 1048–1054.
[39] P. Dong, Y. Wang, B. Cao, S. Xin, L. Guo, J. Zhang, F. Li, Appl. Catal. B: Environ. 132–133 (2013) 45–53.
[40] P. Zhang, L. Wang, X. Zhang, C. Shao, J. Hu, G. Shao, Appl. Catal. B: Environ. 166-167 (2015) 193–201.
[41] L.-W. Zhang, H.-B. Fu, Y.-F. Zhu, Adv. Funct. Mater. 18 (2008) 2180–2189.
[42] A. Bera, D. Basak, ACS Appl. Mater. Interfaces 2 (2010) 408–412.
[43] J. Wang, P. Wang, Y. Cao, J. Chen, W. Li, Y. Shao, Y. Zheng, D. Li, Appl. Catal. B: Environ. 136–137 (2013) 94–102.
[44] W. Wang, J. Yu, Q. Xiang, B. Cheng, Appl. Catal. B: Environ. 119–120 (2012) 109–116.
[45] T. Li, L. Zhao, Y. He, J. Cai, M. Luo, J. Lin, Appl. Catal. B: Environ. 129 (2013) 255–263.
[46] B. Xin, L. Jing, Z. Ren, B. Wang, H. Fu, J. Phys. Chem. B 109 (2005) 2805–2809.
[47] X.Z. Li, F.B. Li, Environ. Sci. Technol. 35 (2001) 2381–2387.
[48] J.-G. Yu, H.-G. Yu, B. Cheng, X.-J. Zhao, J.C. Yu, W.-K. Ho, J. Phys. Chem. B 107 (2003) 13871–13879.
[49] J. Liqiang, Q. Yichun, W. Baiqi, L. Shudan, J. Baojiang, Y. Libin, F. Wei, F. Honggang, S. Jiazhong, Sol. Energy Mater. Sol. Cells 90 (2006) 1773–1787.
[50] J. Yu, L. Qi, M. Jaroniec, J. Phys. Chem. C 114 (2010) 13118–13125.
[51] J. Yu, L. Yue, S. Liu, B. Huang, X. Zhang, J.Colloid Interface Sci. 334 (2009) 58–64.
[52] J. Lin, R. Zong, M. Zhou, Y. Zhu, Appl. Catal. B: Environ. 89 (2009) 425–431.
[53] M. Yan, Y. Hua, F. Zhu, W. Gu, J. Jiang, H. Shen, W. Shi, Appl. Catal. B: Environ. 202 (2017) 518–527.
[54] Q. Liang, Y. Shi, W. Ma, Z. Li, X. Yang, Phys. Chem. Chem. Phys. 14 (2012) 15657–15665.
[55] X. Ma, H. Li, T. Liu, S. Du, Q. Qiang, Y. Wang, S. Yin, T. Sato, Appl. Catal. B: Environ. 201 (2017) 348–358.
[56] L. Wu, F. Li, Y. Xu, J.W. Zhang, D. Zhang, G. Li, H. Li, Appl. Catal. B: Environ. 164 (2015) 217–224.
[57] X. Chen, F. Liu, X. Yan, Y. Yang, Q. Chen, J. Wan, L. Tian, Q. Xia, X. Chen, Chem.-Eur. J. 21 (2015) 18711–18716.
[58] S.J. Hong, S. Lee, J.S. Jang, J.S. Lee, Energy Environ. Sci. 4 (2011) 1781.
[59] H. Yang, J. Tian, T. Li, H. Cui, Catal. Commun. 87 (2016) 82–85.
[60] H. Jia, W. He, W.G. Wamer, X. Han, B. Zhang, S. Zhang, Z. Zheng, Y. Xiang, J.-J. Yin, J. Phys. Chem. C 118 (2014) 21447–21456.